Advanced Powder Technology 29 (2018) 1827–1837

Contents lists available at ScienceDirect

Advanced Powder Technology

journal homepage: www.elsevier.com/locate/apt

Original Research Paper

Synthesis of Ag-AgBr/Al-MCM-41 nanocomposite and its application in photocatalytic oxidative desulfurization of dibenzothiophene

Xuan Nui Pham [a,*], Ba Manh Nguyen [a], Hoa Tran Thi [b], Huan Van Doan [c]

[a] Department of Chemical Engineering, Hanoi University of Mining and Geology, 18 Pho Vien, Duc Thang, Bac Tu Liem district, Hanoi, Viet Nam
[b] Department of Chemical Engineering, Viet Tri University of Industry, 9 Tien Son Str., Viet Tri City, Viet Nam
[c] Department of Mechanical Engineering, University of Bristol, Bristol BS8 1TH, United Kingdom

ARTICLE INFO

Article history:
Received 28 December 2017
Received in revised form 17 April 2018
Accepted 19 April 2018
Available online 3 May 2018

Keywords:
Ag-AgBr/Al-MCM-41
Photocatalysis
Nanocomposite materials
Mesoporous
Dibenzothiophene

ABSTRACT

A series of Ag-AgBr/Al-MCM-41 nanocomposites were synthesized by dispersion of Ag-AgBr on mesoporous silica Al-MCM-41 obtained from natural bentonite. The synthesized Ag-AgBr/Al-MCM-41 composites with Ag nanoparticles growing on the surface of Al-MCM-41 were used for photocatalytic oxidative desulfurization of dibenzothiophene. The physical properties of Ag-AgBr/Al-MCM-41 were characterized by X-ray diffraction (XRD), energy dispersive X-ray spectroscopy (EDS), scanning electron microscopy (SEM), transmission electron microscopy (TEM), Ultraviolet–visible diffuse reflection spectroscopy (UV–Vis DRS), photoluminescence (PL) emission spectra, and X-ray photoelectron spectroscopy (XPS). The photocatalytic activity results showed that in the presence of 40% Ag-AgBr/Al-MCM-41 photocatalyst the oxidative desulfurization of dibenzothiophene reached the maximum efficiency at 99.22% and the photocatalytic activity still keeps high level after four cycles.

1. Introduction

Photocatalysis, in which catalysts are used to enhance the activity of a reaction involving the absorption of light, has been widely utilized in the field of green chemistry, such as wastewater treatment [1], exhaust gas treatment [2], and hydrogen production [3–5]. During the past few decades, TiO_2 has been considered as one of the most promising and suitable photocatalysts in green chemistry technology. TiO_2, however, is only able to use a maximum of 5% of solar energy due to its large band-gap (3.0 and 3.2 eV for rutile and anatase, respectively) [6,7], meaning that it cannot be applied on a large scale. Therefore a simple, effective, and stable photocatalyst needs to be developed to work well in the visible-light region.

The photocatalytic performance of photocatalysts can be improved remarkably thanks to the effect of surface plasmon resonance exhibited by some noble metal nanoparticles, such as Au, Ag, when they are used as co-catalysts. Recently, some photocatalysts with excellent photocatalytic activities have been developed based on surface plasmon resonance, such as Ag/SBA-15 [8], Ag@C_3N_4 [9], and Au/TiO_2 [10]. In addition, plasmonic composites of Ag-AgBr [11-13], Ag–AgCl [14], and Ag/AgI [15,16] have also been reported for their excellent photocatalytic activities. Among these, silver bromide (AgBr) is well known as a narrow band gap (2.6 eV) semiconductor for constructing heterostructured semiconductor systems. Ag-AgBr has been a new visible light photocatalytic material for its good sensitivity to light and stability under visible light irradiation. This is due to the surface plasmon resonance (SPR) of silver nanoparticles produced on the surface of silver bromide [17], and these silver nanoparticles can enhance the electron migration to increase the interfacial charge transfer and inhibit the recombination of electron-hole pair efficiently [13].

However, the photocatalytic activity of Ag-AgBr photocatalysts are limited due to their relatively large, micrometre-sized particles, which lead to low surface areas and high recombination speeds of the photo-generated charge supports [18]. In order to make an efficient use of solar energy for photocatalysis, loading silver bromide onto high surface area supports is considered to be an effective method to improve the ability of photocatalysts for removing organic pollutants by adsorption-photocatalysis. It has been reported that Ag-AgBr can be loaded onto many supports such as activated carbon [19], carbon nanotubes [20], graphene-oxide [21], γ-Al_2O_3 [16], and TiO_2 [22,23]. Until now, nanostructured silver/silver halides, including nanowires, microspheres, or nanotubes, have been synthesized by a variety of methods [24–26]. Template-based synthesis method has been attracted many scientists because this method utilizes a pre-existing guide with desired

* Corresponding author.
E-mail address: phamxuannui@humg.edu.vn (X.N. Pham).

https://doi.org/10.1016/j.apt.2018.04.019

nanoscale features to direct the formation of nanomaterials into forms that are difficult to achieve by other methods [27]. Wang et al. reported the synthesis of porous AgBr/Ag composite microspheres using a one-step template-assisted in-situ route [28] and Ag-AgBr composite nanoparticles through ion-exchange of Ag_2MoO_4 template with HBr [11]. Xiao et al. prepared Ag@AgBr cubic cages using a water-soluble sacrificial salt-crystal-template process [13]. In addition, cetyltrimethylammonium bromide (CTABr) is known as an effective template, and has been widely used in the morphology-controlled synthesis of nanoparticles [29]. Typically, CTABr and $AgNO_3$, have been used to prepare AgBr nanoparticles on a matrix, and then a part of the Ag^+ in silver bromide is reduced to metallic Ag particles by light irradiation. However, a popular method of dispersing Ag-AgBr on a support easily results in the accumulation of active particles on the surface of the support, which often destroy the support's channel structures, hence decreasing the adsorption-photocatalysis performance of this composite.

In this study, we prepared a novel nanocomposite Ag-AgBr/Al-MCM-41 with excellent photocatalytic activity by loading Ag-AgBr on Al-MCM-41 from natural bentonite as silica and aluminum sources using the chemical deposition. The photocatalytic performance of Ag-AgBr/Al-MCM-41 was assessed with different contents of Ag-AgBr synthesized using cetyltrimethyl ammonium bromide (CTAB). The photocatalytic activity of the nanocomposite was tested in the context of its oxidative desulfurization of dibenzothiophene as a model fuel in the presence of H_2O_2 under UV radiation. The effect of Ag-AgBr content on the photocatalytic activity of the nanocomposite was thereby investigated in detail.

2. Experimental

2.1. Materials

The natural bentonite with a chemical composition of 54.22 SiO_2; 15.8 Al_2O_3; 11.08 Fe_2O_3; 0.84 TiO_2; 2.07 CaO; 3.56 MgO; 1.98 Na_2O in weight percent, and the loss on ignition (LOI) of 10.45%, was obtained from Di Linh, Vietnam. All other reagents and chemicals including cetyltrimethylammonium bromide (CTAB, ≥98%), hydrochloric acid (HCl, 37%), nitric acid (HNO_3, 69%), sodium hydroxide (NaOH, 97%, pellets), hydrogen peroxide (H_2O_2, 30% in water), silver nitrate ($AgNO_3$, ≥98%), dibenzothiophene (DBT, 98%), and *n*-octane (98%) were obtained from Sigma–Aldrich without further purification.

2.2. Synthesis of Al-MCM-41 from Vietnamese bentonite

Al-MCM-41 was synthesized following studies reported by Yang *et al.* and Ali-dahmane *et al.* [30,31]. In this synthesis procedure, a mixture of 1 bentonite:1.2 NaOH powder in weight ratio was calcined in air at 600 °C for 5 h. The fused mixture was cooled down to room temperature, then stirred vigorously in distilled water for 24 h. The resultant suspension was separated to obtain a supernatant containing silica and aluminum. In the next step, 1.2 g of CTAB was dissolved into 20 mL of distilled water. This mixture then was added up by 80 mL above supernatant under stirring. After 15 mins, HNO_3 2M was dropped into the mixture to adjust pH of 10, then stirred for another 2 h. The resultant slurry achieved after this reaction was transferred to a Teflon-lined stainless-steel autoclave (250 mL) and aged at 110 °C for 24 h. After crystallization, the white solid obtained was filtered, washed repeatedly with distilled water and dried at 100 °C overnight. Finally, the sample was calcined in a furnace at 550 °C for 5 h with a heating rate of 2 °C/min to form Al-MCM-41.

2.3. Synthesis of Ag-AgBr/MCM-41 nanocomposites by chemical vapor deposition method

An appropriate amount of Al-MCM-41, CTAB, and $AgNO_3$ were placed in each side of a quartz reactor with the glass wool placed in the middle of the wall. Nitrogen was introduced slowly to reaction tube with a rate of 60 mL/min for 15 min to remove all the oxygen present in the reaction system. The reactor was then heated up to 400 °C for 3 h with a ramping rate of 10 °C/min (Scheme 1). The desired amount of Ag-AgBr in the catalyst was adjusted by varying $AgNO_3$ content. Bromide ion in CTAB was used in excess amounts to effectively precipitate AgBr. A series of Ag-AgBr/Al-MCM-41 samples with different amount of Ag-AgBr ranging from 10 to 60% were labeled as x% Ag-AgBr/Al-MCM-41 with x is the weight percentage of Ag-AgBr in the samples.

2.4. Characterization techniques

The crystalline phase structure of as-prepared materials was determined over the 2-theta range of 1–10° and 10–80° (D8 ADVANCE, Bruker, Germany) using Cu $K\alpha_1$ copper radiation ($\lambda = 0.154$ nm) as the X-ray source at a scan rate of 3° min^{-1}. The Brunauer–Emmett–Teller (BET) surface areas of the samples were

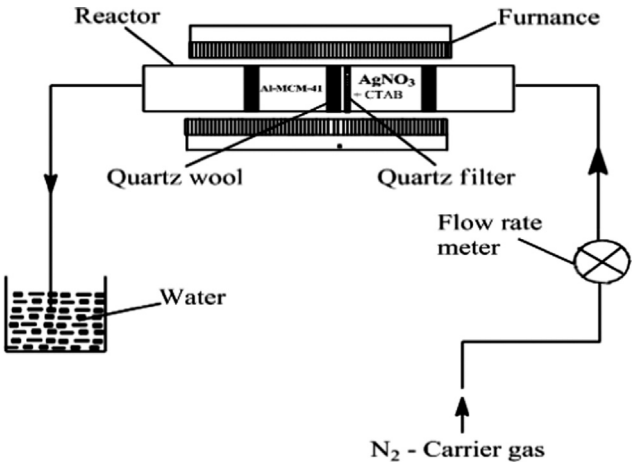

Scheme 1. Reactor setup for the chemical deposition process.

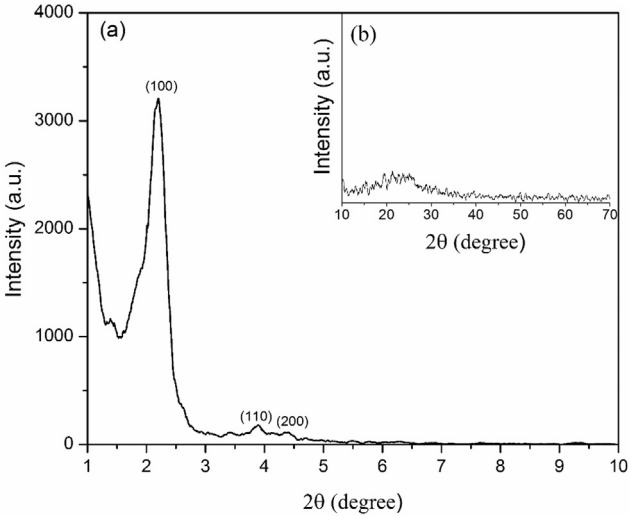

Fig. 1. (a) Small-angle and (b) wide-angle XRD patterns of the synthesized Al-MCM-41 from bentonite.

evaluated by the N_2 adsorption isotherm at 77 K using a BET Sorptometer (Automated Sorptometer BET 201-A, USA). The morphology of the nanocomposites was observed by SEM using an S-4800 microscope (Hitachi, Japan), operating at an accelerating Voltage of 200 kV. The transmission electron microscopy (TEM) analysis was performed on a Leica IEO 906E microscope operating at 120 kV, and the samples were prepared by suspending in ethanol. Energy-dispersive X-ray spectroscopy analysis (EDX) was measured on a JED-2300 with gold coating. The surface electronic state was identified through X-ray photo-electron spectroscopy (XPS) performed on an AXISULTRA DLD Shimadzu Kratos Spectrometer (Japan) using monochromated Al K_α radiation (1486.6 eV). The PL spectra of the photocatalysts were detected using a spectrofluorometer Fluorolog FL3-22 JobinYvon-Spex, USA using a 450W xenon lamp as an excitation source with excitation wavelength of 400 nm. UV-Vis diffuse reflection spectroscopy (DRS) was performed on a Shimadzu UV2550 spectrophotometer with $BaSO_4$-coated integrating sphere in the wavelength range of 200–800 nm.

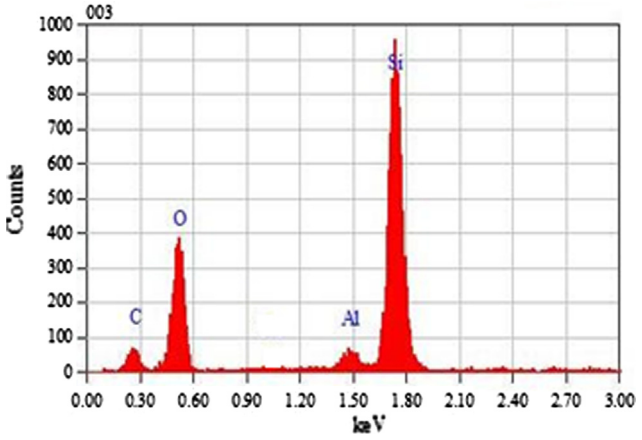

Fig. 2. EDS spectrum of Al-MCM-41.

2.5. Photocatalytic oxidative desulfurization of dibenzothiophene (DBT)

Photocatalytic activity of Ag-AgBr/Al-MCM-41 nanocomposite was determined by photocatalytic oxidative desulfurization of a model fuel. This fuel was prepared by adding 0.5 g of DBT in 1L of *n*-octane to get 500 pmm DBT solution. Then 10 mL of model fuel and 0.2 g of Ag-AgBr/Al-MCM-41 photocatalyst were placed into the reactor. Before illumination, the suspension was placed in the dark for 45 min to attain adsorption-desorption equilibrium between the photocatalyst and DBT under constant stirring. After that, an appropriate amount of H_2O_2 was added into the reaction system and it was illuminated with the 125 W high pressure Hg

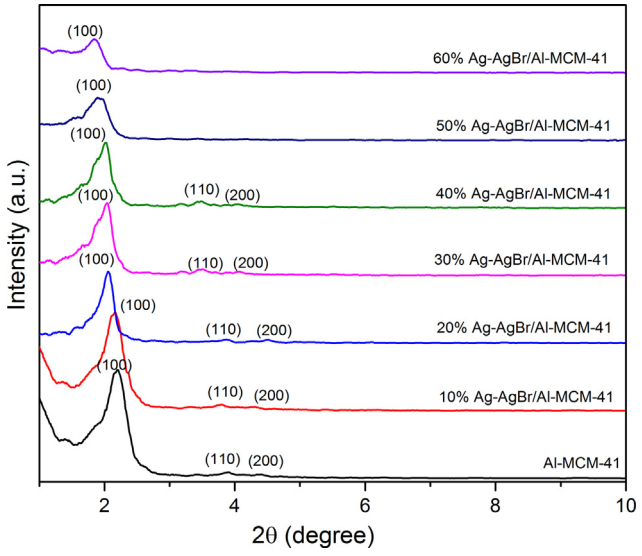

Fig. 3. Small-angle XRD patterns of 10–60% Ag-AgBr/Al-MCM-41.

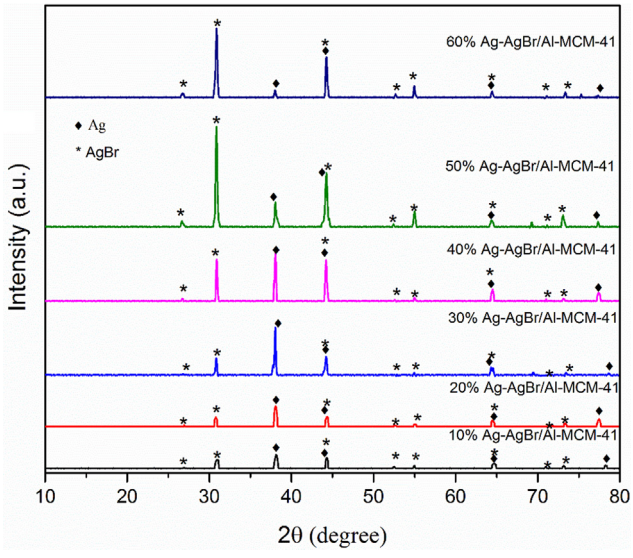

Fig. 4. Wide-angle XRD patterns of 10–60% Ag-AgBr/Al-MCM-41.

Table 1
Textural properties of Al-MCM-41 and Ag-AgBr/Al-MCM-41 samples.

Samples	S_{BET} (m^2/g)	V_{pore} (cm^3/g)	D (nm)	d_{100} (Å)	a_0 (nm)
Al-MCM-41	633	0.94	8.64	36.85	4.25
10% Ag-AgBr/Al-MCM-41	623	0.79	8.55	37.28	4.30
20% Ag-AgBr/Al-MCM-41	571	0.75	8.23	37.59	4.34
30% Ag-AgBr/Al-MCM-41	479	0.74	7.20	38.37	4.43
40% Ag-AgBr/Al-MCM-41	478	0.66	7.05	39.11	4.52
50% Ag-AgBr/Al-MCM-41	237	0.55	4.68	40.28	4.65
60% Ag-AgBr/Al-MCM-41	114	0.36	4.56	40.94	4.73

S_{BET}: Specific surface area calculated by the BET method.
D_p: Pore diameter and V_p: Pore volume calculated from the N_2 desorption data based on the BJH method.
d_{100}, the space distance between (*100*) planes.
a_o, lattice cell parameter of the hexagonal structure.
Unit-cell parameter determined from the position of the (*100*) diffraction line as $a_o = 2d_{100}\sqrt{3}$.
Pore wall thickness calculated as $w = a_o - D_p$.

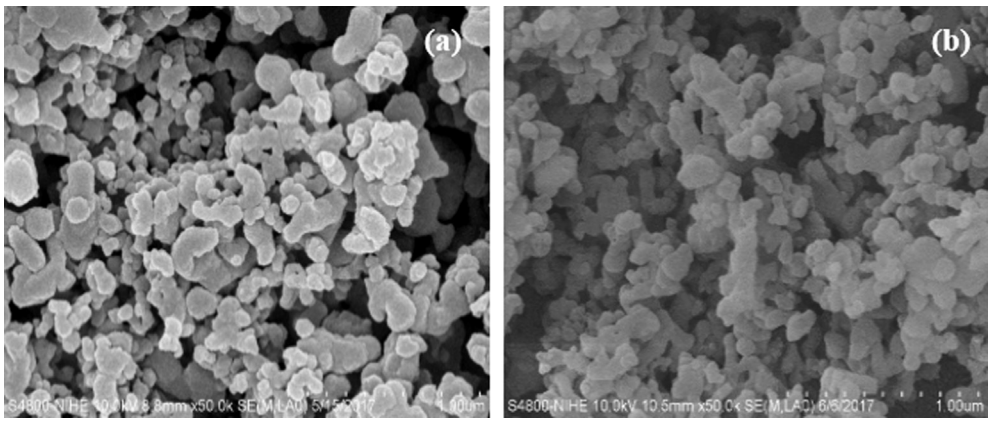

Fig. 5. SEM images of (a) Al-MCM-41 and (b) 40% Ag-AgBr/Al-MCM-41.

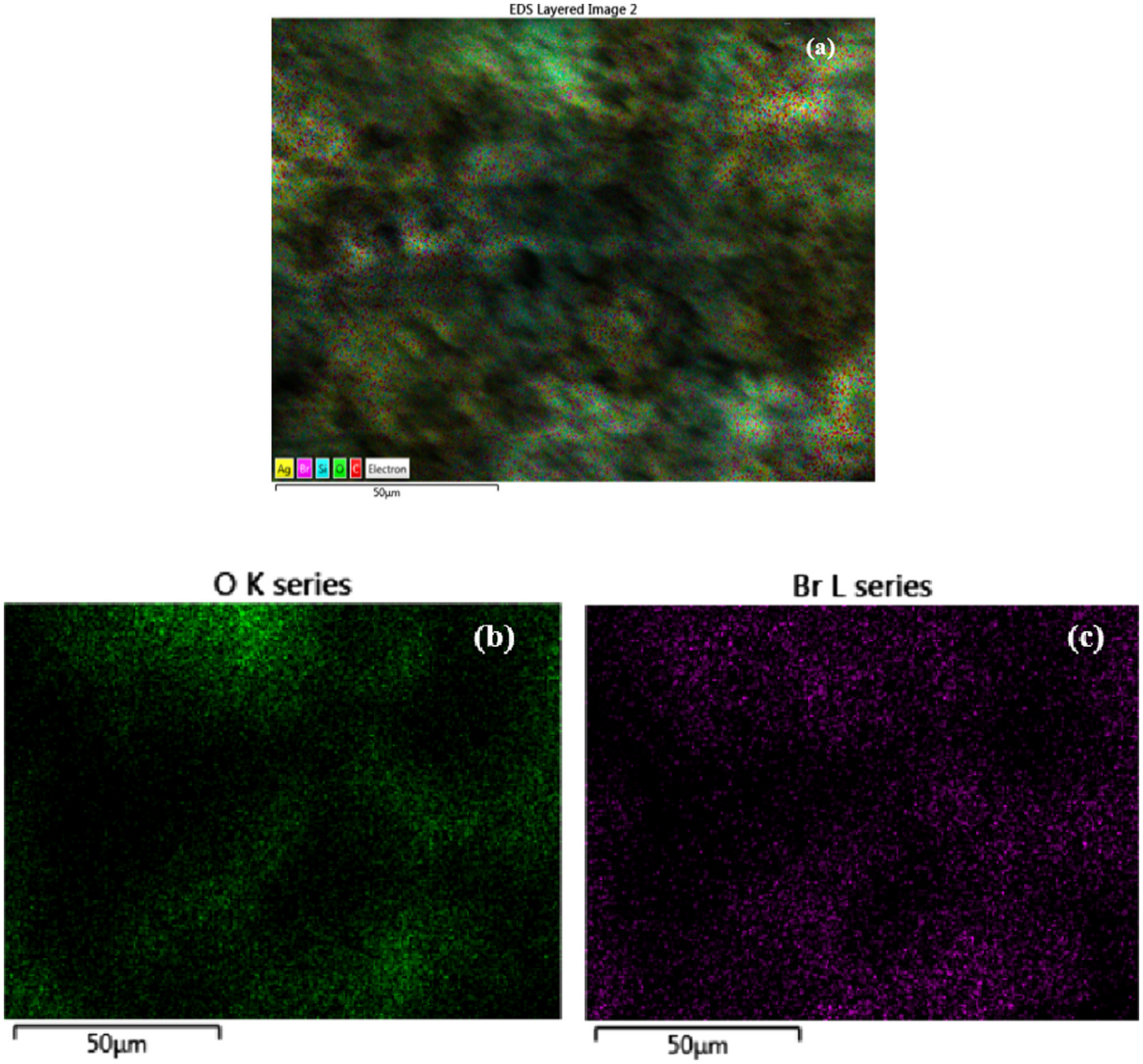

Fig. 6. EDS elemental mapping analysis of 40% Ag-AgBr/Al-MCM-41, (a) the SEM image of the analyzed sample, (b) the yellow color represents element Ag, (c) the purple color is element Br.

lamp. The absorption of DBT was monitored with a UV-Vis spectrophotometer at λ_{max} = 325 nm [32].

The strong absorption at this wavelength suggested an $n \rightarrow \pi^*$ excitation similar to that for the sulfur atom in DBT. The conversion of DBT was calculated according to the initial, C_o (mg L^{-1}), and final, C_t (mg L^{-1}) concentrations of DBT in the reaction solution at reaction time t (min).

$$\chi = ((C_o - C_t)/C_o) \times 100$$

where χ is the conversion percent of DBT.

3. Results and discussion

3.1. Characterizations of the nanocomposites

The small and wide angle XRD patterns of different samples are shown in Fig. 1a and b, respectively. Al-MCM-41 (Fig. 1a) exhibits a strong diffraction peak and two obvious sub-peaks corresponding to the diffraction planes (1 0 0), (2 0 0), and (2 1 0), respectively, which indicates Al-MCM-41 synthesized from Vietnamese bentonite possesses a typical two-dimensional hexagonal lattice and hexagonal channels of MCM-41 material [33]. Moreover, no characteristic peaks of amorphous silicon phase or impurity at 2θ = 10–40°, suggesting major amounts of silicon and aluminum extracted from the bentonite were consumed to produce Al-MCM-41 (see Fig. 2).

Three elements including O, Si and Al in Al-MCM-41 sample were detected by EDS method. The signal of C in the spectrum is derived from the carbon used to support the specimen.

Small-angle XRD patterns of all composite samples with 10–60% Ag-AgBr were showed in Fig. 3. The peak of the (1 0 0) crystal plane at 2θ between 1.9 and 2.4° observed in these results is for Al-MCM-41, indicating that the well-fined ordered structure of the mesoporous material remained unchanged. However, the peak intensity of Ag-AgBr/Al-MCM-41 decreases while the amount of Ag-AgBr depositing on Al-MCM-41 increases. This could be due to the difference on the scattering contrasts of Ag and AgBr being self-assembled into mesoporous channel of Al-MCM-41. This results is in good agreement what stated in previous studied by Maler and Yang et al. [34,35]. Indeed, it can be seen that Ag-AgBr was successfully loaded on the surface of Al-MCM-41 accompanied by increasing the amount of Ag-AgBr from 10–40%. However, the (1 1 0) and (2 0 0) planes correlated with 2θ = 3.8° and 4.4° of Ag-AgBr/Al-MCM-41 completely disappear when the amount of Ag-AgBr increased from 50% to 60%. It demonstrates that the increasing amount of Ag-AgBr has covered part of porous structure and decreased intensity of diffraction peaks of (1 0 0), (1 1 0), and (2 0 0) planes of Al-MCM-41 support.

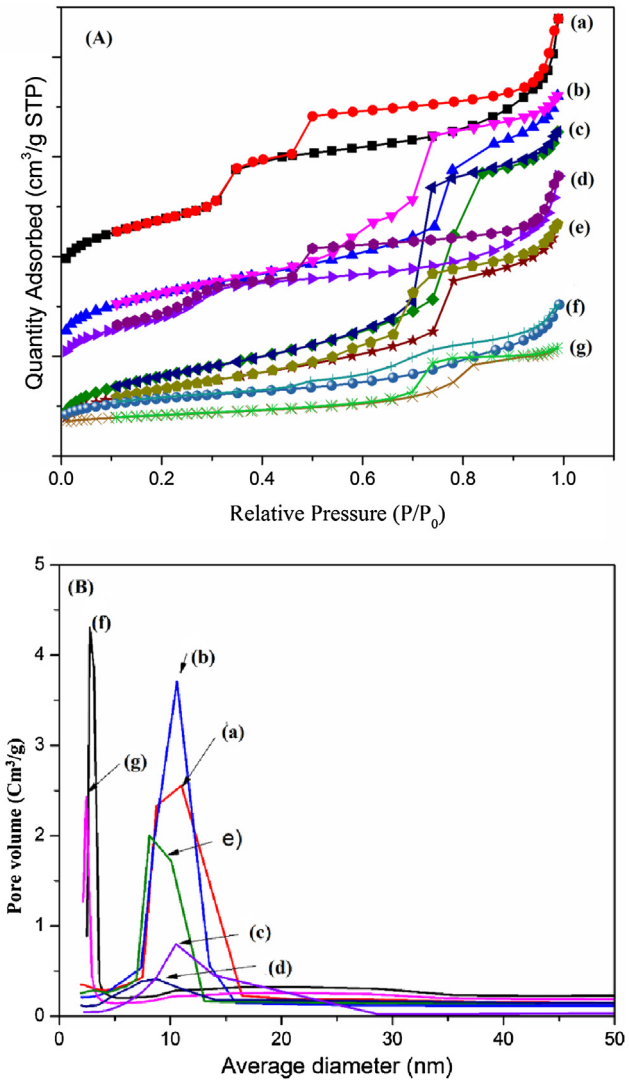

Fig. 8. (A) Nitrogen adsorption-desorption isotherms, (B) BJH pore size distribution of: (a) Al-MCM-41, (b) 10% Ag-AgBr/Al-MCM-41, (c) 20% Ag-AgBr/Al-MCM-41, (d) 30% Ag-AgBr/Al-MCM-41, (e) 40% Ag-AgBr/Al-MCM-41, (f) 50% Ag-AgBr/Al-MCM-41, (g) 60% Ag-AgBr/Al-MCM-41.

Additionally, in the presence of Ag-AgBr, the (1 0 0) diffraction peak shifts to lower 2θ value, results in the slight increase of a_o parameter of the mesostructure network ($a_0 = 2d_{100}/\sqrt{3}$) (Table 1). This increase may be related to the metallic ion (Ag^+) substitution

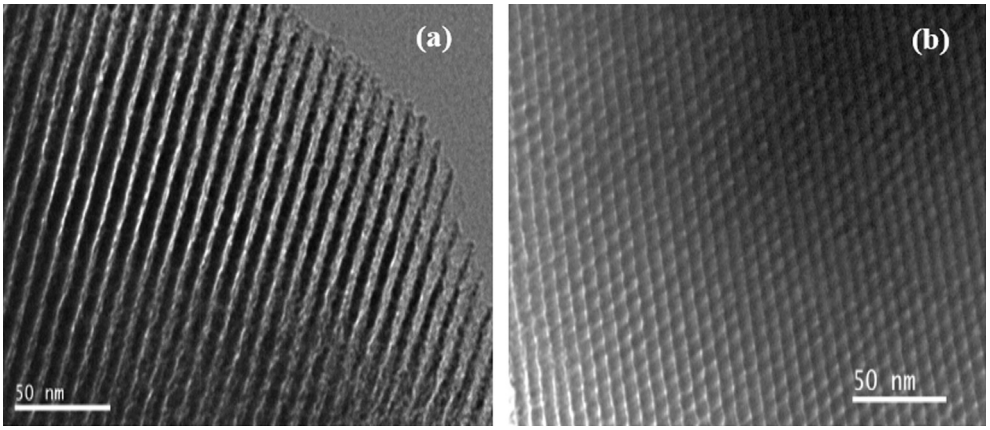

Fig. 7. TEM images of 40% Ag-AgBr/Al-MCM-41.

with Si^{4+} in the Al-MCM-41 network. Since the ionic radius of Ag^{+} (0.61) is greater than that of Si^{4+} (0.41), the Ag—O bonding length is greater than that of Si—O, which leads to the increase in a_o parameter of the network [36–38].

Wide-angle diffraction reflections (Fig. 4) at 26.7°, 31°, 44.3°, 55°, 64.5°, and 73.4° were designated respectively to (1 1 1), (2 0 0), (2 2 0), (2 2 2), (4 0 0), and (4 2 0) planes of cubic AgBr (JCPDS No. 06-0438). The reflections at 38.1°, 44.3°, and 64.5° were assigned to the (1 1 1), (2 0 0), and (2 2 0) planes of metallic Ag (JCPDS No.04-0783) [39,40]. In addition, the intensities of these diffraction peaks were constantly enhanced, thus indicated a better crystallinity with the increase of AgBr content.

SEM images of Al-MCM-41 revealed irregular spherical particles with a cross-linked network (Fig. 5a). Fig. 5b shows the self-assembling of Ag-AgBr particles on the surface and into the mesoporous channels of Al-MCM-41. The obtained nanocomposite exhibited a uniform coverage of Ag-AgBr particles while retaining its good mesoporous structure.

Fig. 6 represents the SEM images of the regions where electron mapping was performed. The yellow and purple colors in Fig. 6a and b correspond to the mapping of silver and bromine elements in the nanocomposite sample, respectively.

The TEM images of the synthesized 40% Ag-AgBr/Al-MCM-41 sample are shown in Fig. 7. The TEM images confirm that the nanocomposite has a well-ordered mesoporous channel arranged in hexagonal structure. This structural ordering is visible in the directions perpendicular (Fig. 7a) and parallel to the pore axis (Fig. 7b). This is consistent with the results obtained from XRD study.

The porosity properties of 10–60% Ag-AgBr/Al-MCM-41 samples are mesoporous materials as characterized by their nitrogen adsorption-desorption isotherms of type IV with hysteresis loop (Fig. 8). The adsorption amount of 40% Ag-AgBr/Al-MCM-41 rose remarkably at a relative low pressure ($P/P_o < 0.4$) compared to 50–60% Ag-AgBr/Al-MCM-41. This could be due to the large specific surface area of 40% Ag-AgBr/Al-MCM-41 promoting monolayer adsorption of nitrogen towards the walls of the mesopores. Moreover, the adsorption amount of Ag-AgBr/Al-MCM-41 decreased dramatically at the pressure range of 0.4–1.0 when the amount of Ag-AgBr increased to 50–60%. This result indicates that the reduction in the pore size of 50–60% Ag-AgBr/Al-MCM-41 samples is due to the high loading of AgBr species into the channel of Al-MCM-41 as well as reduced degree of order in the mesoporous structure . Indeed, no major difference in adsorption isotherms of 40% Ag-AgBr/Al-MCM-41 and Al-MCM-41 was observed, which indicates that 40% Ag-AgBr has a mesoporous structure. The specific surface area, pore volume, and pore diameter of all samples are listed in Table 1.

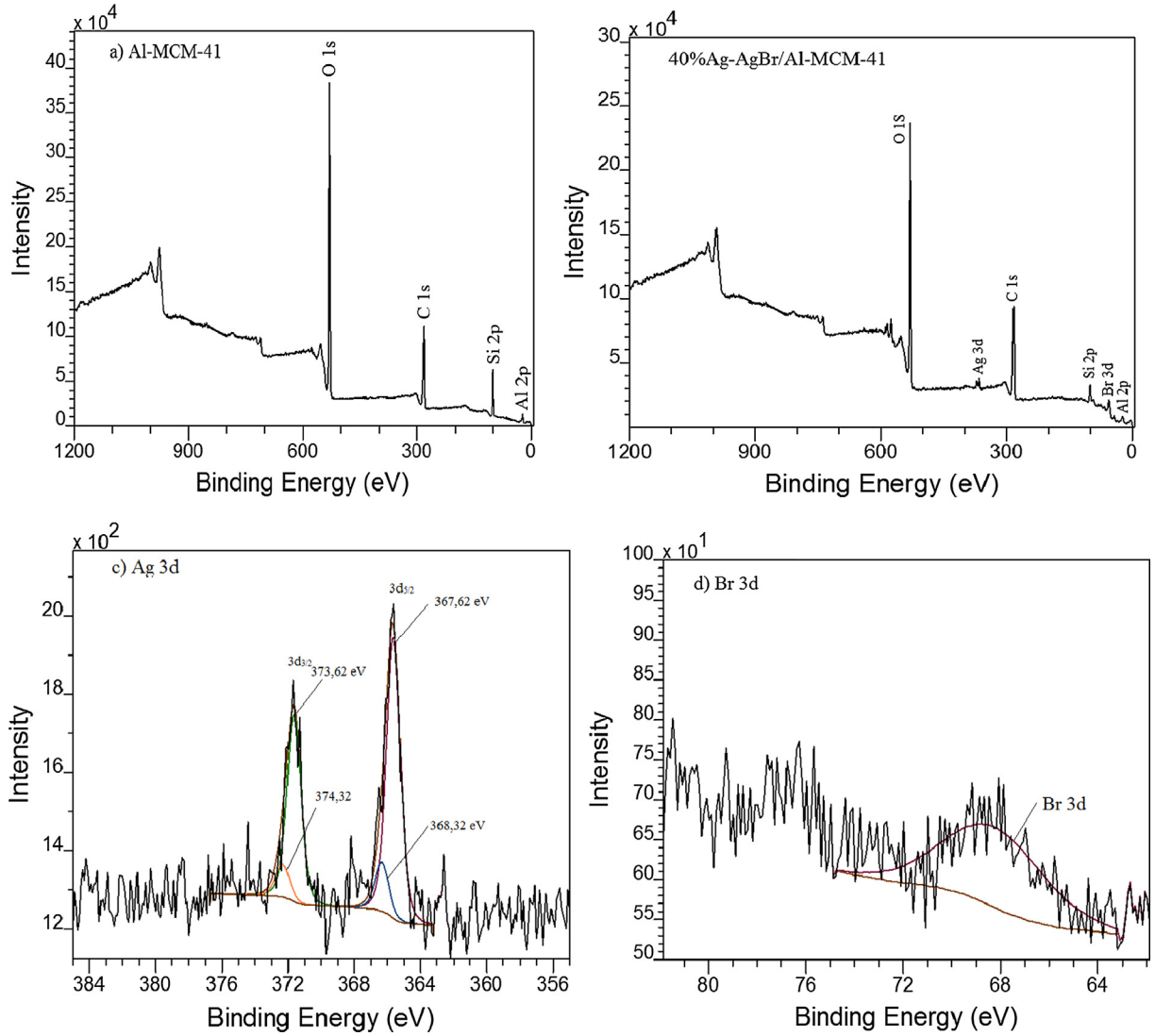

Fig. 9. XPS spectra of (a) Al-MCM-41, (b) 40% Ag-AgBr/Al-MCM-41, and high-resolution XPS spectra of Ag 3d (c) and Br 3d (d) of 40% Ag-AgBr/Al-MCM-41.

XPS spectra of Al-MCM-41 and 40% Ag-AgBr/Al-MCM-41 nanocomposites are shown in Fig. 9. The peaks assigning to Ag 3d, Br 3d, Si 2p, O 1s, and Al 2p are presence in the spectra of the two samples, except for the C 1s peak arising from adventitious hydrocarbon in the XPS instrument. Fig. 9c showed two bands at 367.62 eV and 373.2 eV are typical for Ag $3d_{5/2}$ and Ag $3d_{3/2}$, respectively. These two bands could be divided into four different peaks: two peaks at 368.32 eV and 374.32 eV are attributed to the Ag^+ in AgBr, while the other two peaks at 373.62 eV and 367.62 eV belong to Ag^o species [41]. The peak at 68.27 eV (Fig. 9d) could be assigned to Br^- in AgBr [42].

The UV-Vis DRS in the wavelength range of 200–800 nm for 10–60% Ag-AgBr/Al-MCM-41 are shown in Fig. 10. Among samples with different amount of Ag-AgBr, 40% Ag-AgBr/Al-MCM-41 sampleshows a superior capacity of light absorption (Fig. 10d). The band-gap energy of a photocatalyst could be calculated using the following equation.

$$\alpha h\nu = (Ah\nu - E_g)^{\frac{n}{2}} \quad (1)$$

where E_g is the band gap (eV), h is the Planck's constant, A is the absorption constant, ν is the light frequency, and (α) is the absorption coefficient. N depends on the characteristics of the transition in a semiconductor, for example n = 1, 4 for direct and indirect transitions, respectively. The band-gap energy E_g can be estimated from the x-axis intercept of the tangent of $(\alpha h\nu)^{1/2}$ plot versus the photon energy (hν).

The band-gap energy E_g calculated from Eq. (1) of 10% Ag-AgBr/Al-MCM-41, 20% Ag-AgBr/Al-MCM-41, 30% Ag-AgBr/Al-MCM-41,

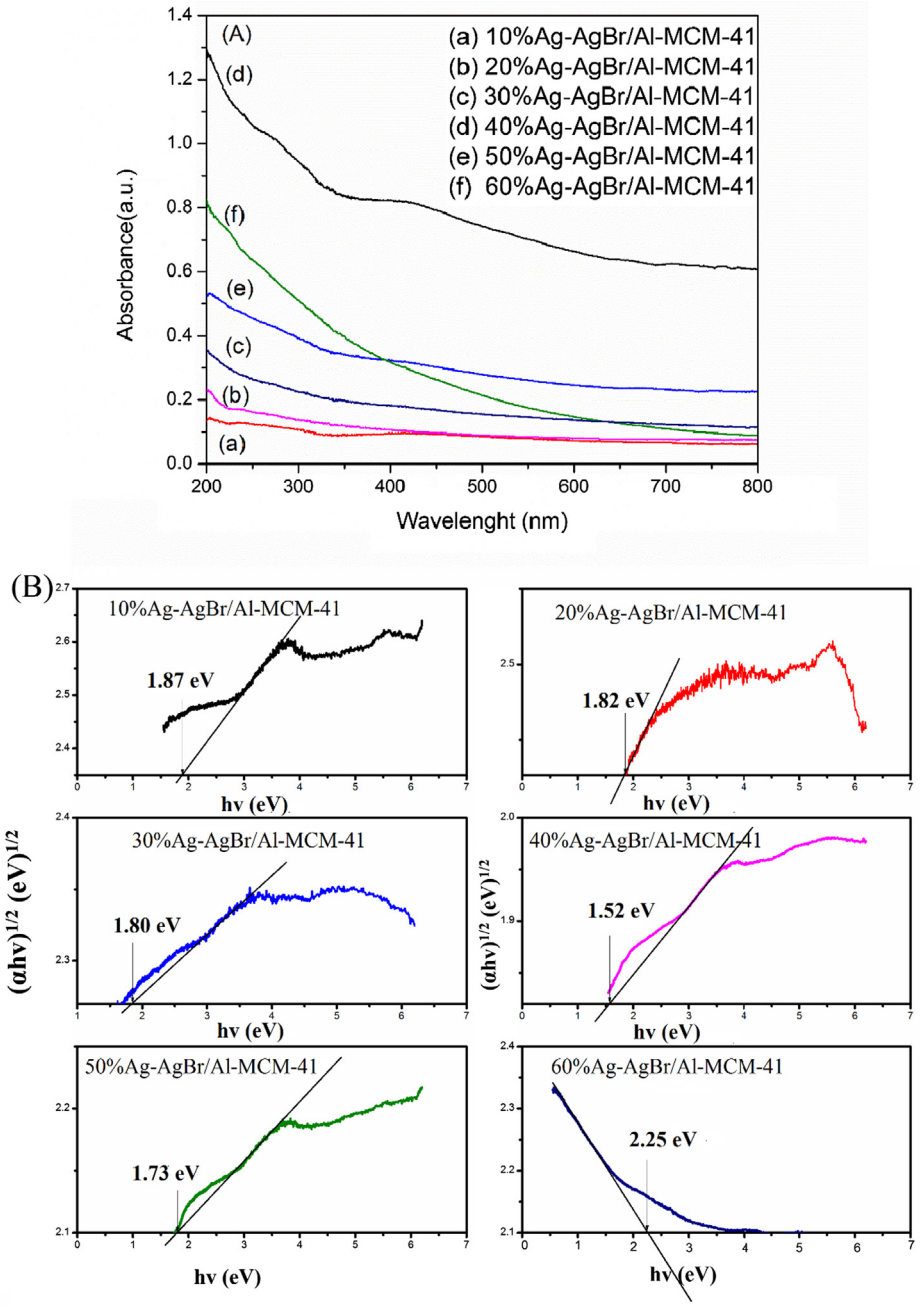

Fig. 10. (A) UV-Vis diffuse reflectance spectra (B) Band-gap energies (E_g) of samples: 10% Ag-AgBr/Al-MCM-41, 20% Ag-AgBr/Al-MCM-41, 30% Ag-AgBr/Al-MCM-41, 40% Ag-AgBr/Al-MCM-41, 50% Ag-AgBr/Al-MCM-41, and 60% Ag-AgBr/Al-MCM-41.

40% Ag-AgBr/Al-MCM-41, 50% Ag-AgBr/Al-MCM-41, and 60% Ag-AgBr/Al-MCM-41 samples are approximately 1.87, 1.82, 1.80, 1.52, and 1.73 eV, respectively. These results are in good agreement with their capacities of light absorption.

In order to further investigate the recombination behavior of the photocatalysts, the PL spectra were obtained using A 450W xenon lamp was applied as an excitation source with the excitation wavelength of 400 nm. The results are shown in Fig. 11.

In this Figure, it is clear to note that the emission band of photocatalyst samples centered at λ = 457 nm. The PL emission intensities significantly decreased with the introduction of Ag@AgBr content from 10% to 40%, and then dramatically increased when the loadings were over 40%. The results demonstrated that the lower levels of Ag-AgBr are enough to provide the appropriate amount of the photogenerated electron–hole pairs and effectively improve the charge transfer and separation. However, when the content of Ag-AgBr is too high, a huge amount of trapping sites could be created and consequently facilitated the recombination of photo-production carriers. As a result, the photocatalytic activity decreased in this case [43].

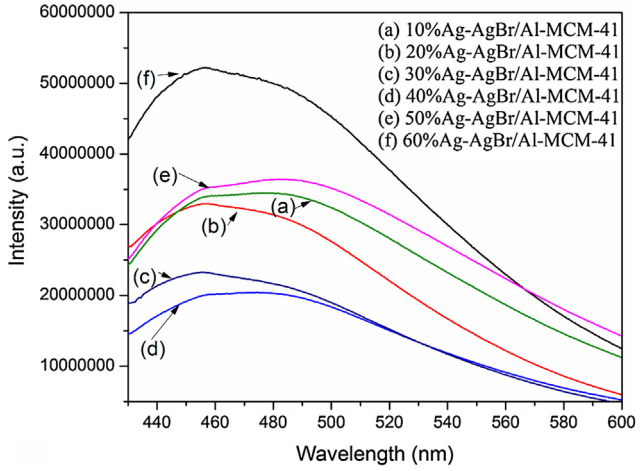

Fig. 11. Photoluminescence (PL) spectra of Ag-AgBr/Al-MCM-41 photocatalysts.

3.2. Photocatalytic activity of the samples

Figs. 12 and 13 illustrate the photocatalysis of 10–60% Ag-AgBr/Al-MCM-41 samples for the desulfurization of DBT under visible-light irradiation. The experiments were conducted at 50 °C and 70 °C, 500 ppm of DBT, 50 mL of dibenzothiophene in *n*-octane solution, and 50 mg of photocatalyst, and 1 mL of H_2O_2.

The results indicate that increasing Ag-AgBr contents from 10% to 40% leads to an increase in the desulfurization rate from 41% to 75% at 50 °C, and from 78% to 98% at 70 °C. However, by increasing Ag-AgBr contents to 50–60%, the conversion of DBT decreases to 51% and 70% at 50 °C and 70 °C, respectively. This could be due to nuch lower surface areas and pore volumes of 56%, 60% Ag-AgBr/Al-MCM-41 samples compared to other catalysts (Table 1). The catalyst of 40% Ag-AgBr/Al-MCM-41 shows the highest photocatalytic activity (Figs. 12 and 13) because it has the lowest band gap energy and a comparably high surface area as 10–30% Ag-AgBr/Al-MCM-41catalysts.

The conversion of DBT is a maximum of 98% at 70 °C. At this temperature, the generation rate of hydroxyl radicals (·OH) is

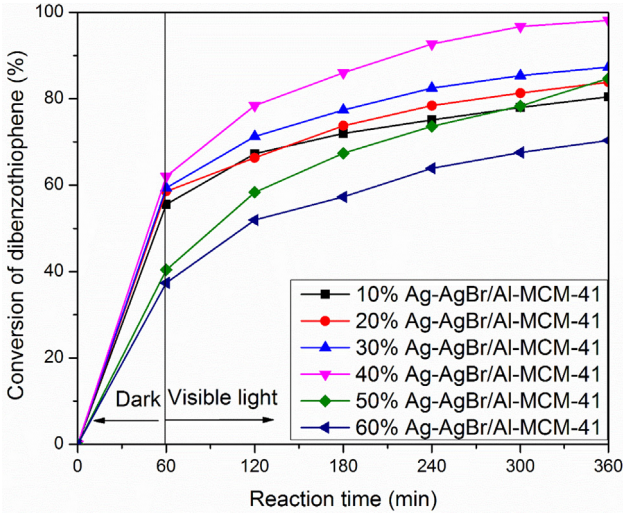

Fig. 13. Conversion of DBT over 10–60% Ag-AgBr/Al-MCM-41 photocatalysts at 70 °C, $V_{model\ oil}$ = 50 mL, $m_{catalyst}$ = 50 mg, and V_{H2O2} = 1 mL.

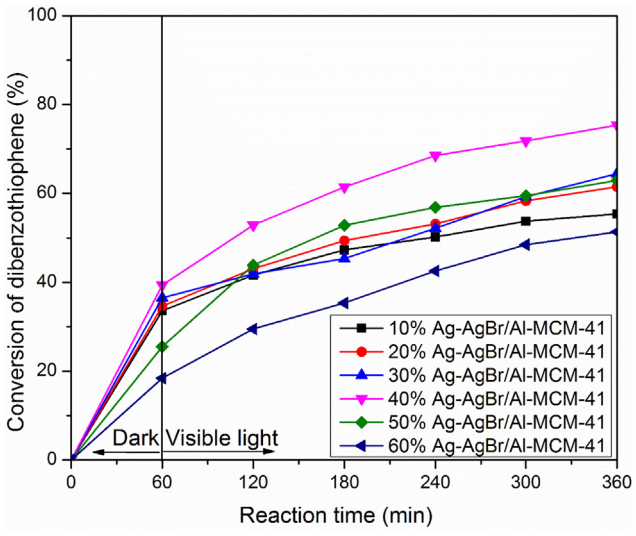

Fig. 12. Conversion of DBT over 10–60% Ag-AgBr/Al-MCM-41 photocatalysts at 50 °C, $V_{model\ oil}$ = 50 mL, $m_{catalyst}$ = 50 mg, and V_{H2O2} = 1 mL.

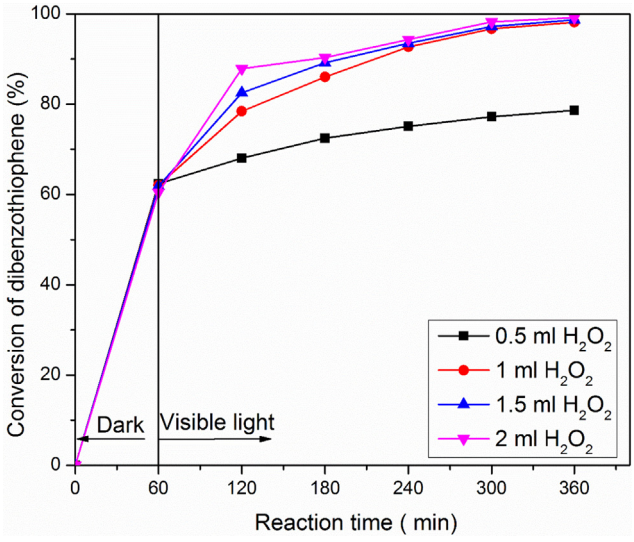

Fig. 14. Conversion profile of DBT at different H_2O_2 oxidant amounts. Experimental conditions: $V_{model\ oil}$ = 20 mL; $m_{40\%Ag\text{-}AgBr/Al\text{-}MCM\text{-}41}$ = 50 mg; t = 70 °C.

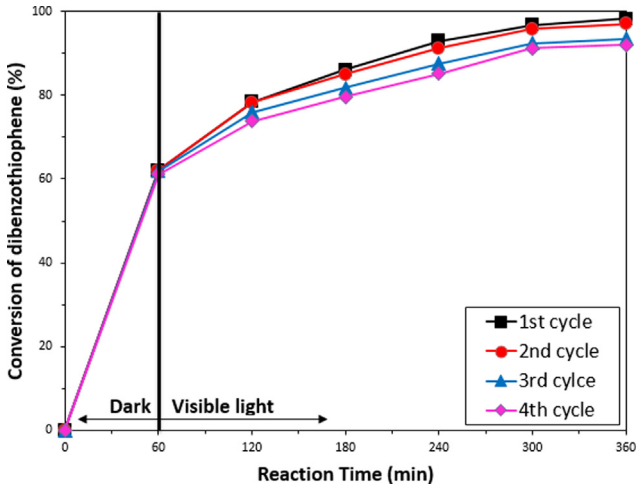

Fig. 15. Conversion of DBT in the presence of 40% Ag-AgBr/Al-MCM-41 for four cycles. Experimental conditions: $V_{model\ oil}$ = 20 mL; $m_{40\%Ag\text{-}AgBr/Al\text{-}MCM\text{-}41}$ = 50 mg; V_{H2O2} = 1 mL; t = 70 °C.

higher than that at 50 °C, thus gives higher conversion of DBT via oxidation on the catalyst surface [44,45]. In addition, the oxidation of DBT below 50 °C is limited by kinetics because of the diffusion restriction at low temperatures.

Fig. 14 showed that the desulfurization conversion of DBT over 40% Ag-AgBr/Al-MCM-41 catalyst after 6 hours reached 78% with the addition of 0.5 mL H_2O_2. The overall conversions of DBT desulfurization remained nearly the same with increasing H_2O_2 concentration from 1 to 2 mL, and reached the highest sulfur removal rate of 98% after 6 h. As already known, H_2O_2 is a strong oxidizing agent that produces hydroxyl radicals when exposure to the light (Eq. (2)). However, an excessive amount of H_2O_2 would poison the Ag-AgBr/Al-MCM-41 catalyst surface, thus has adverse effect to the photocatalytic reaction [46].

$$H_2O_2 \xrightarrow{h\nu} 2{\cdot}OH \quad (2)$$

This resulted inan optimal amount of hydroxyl radicals for the oxidation of DBT obtained with the addition of approximately 1 mL H_2O_2. When H_2O_2 was used at low concentration (<0.5 mL), the reaction between the hydroxyl radicals and H_2O_2 are given in Eq. (3):

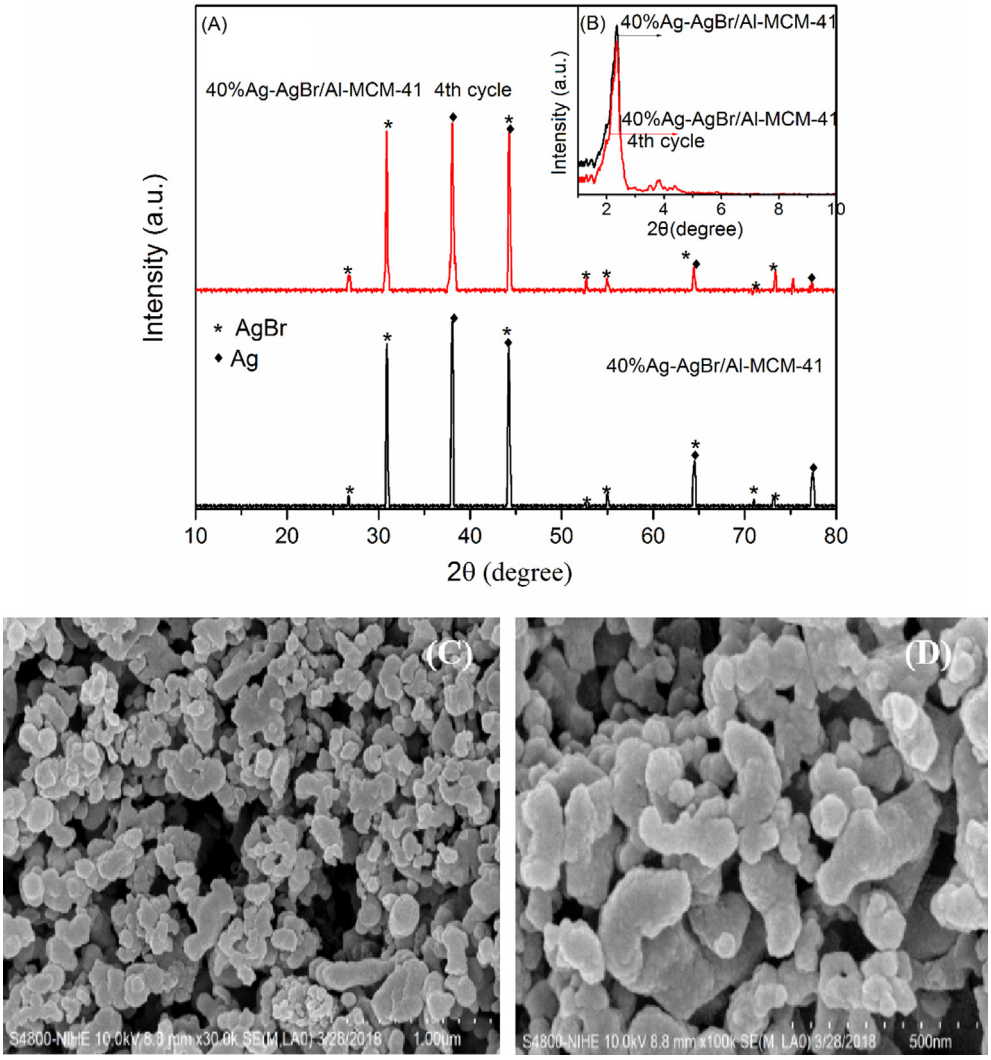

Fig. 16. XRD patterns of 40% Ag-AgBr/Al-MCM-41 photocatalyst before (A) and after (B) oxidative desulfurization; (C and D) the SEM images of 40% Ag-AgBr/Al-MCM-41 after oxidative desulfurization.

$$H_2O_2 + \cdot OH \rightarrow H_2O + O_2^- + H^+ \quad (3)$$

is minimized, while the need to provide sufficient radicals is neccesary to facilitate the oxidation reaction. Therefore, activity of Ag-AgBr nanoparticles on the support of Al-MCM-41 for DBT photodegradation largely depends on the photo-generated electron-hole pairs. AgBr and Ag^o could be excited by ultraviolet due to the band-gap structure and surface plasmon resonance, respectively. Firstly, AgBr can be excited to form photo-generated electron-hole pairs according to Eq. (4):

$$AgBr + h\nu \rightarrow AgBr(e^- + h^+) \quad (4)$$

The Ag^o nanoparticles on the surface of Ag-AgBr/Al-MCM-41 could act as electron traps to facilitate the separation of photo-generated electron hole pairs as following:

$$AgBr(e^-) + Ag \rightarrow AgBr + Ag(e^-) \quad (5)$$

These photo-generated electrons reactwith anion oxygen O_2^- (from Eq. (3)) absorbed on the catalyst surface to produce strong oxidizing and active ($\cdot O_2^-$) as equation.

$$Ag(e^-) + O_2^- \rightarrow \cdot O_2^- + Ag \quad (6)$$

Simultaneously, the holes left on the valence band of AgBr can react with H_2O molecules (from Eq. (3)) to generate ·OH as below equation:

$$AgBr(h^+) + H_2O \rightarrow \cdot OH + AgBr + H^+ \quad (7)$$

or $AgBr(h^+)$ oxidize Br^- to form Br^o as [43,47]:

$$AgBr(h^+) + Br^- \rightarrow Br^o + AgBr \quad (8)$$

Therefore, the surface active species such as $\cdot O_2^-$, h^+, ·OH and Br· play an important role in the oxidative desulfurization of DBT.

The stability of the catalyst is an important factor of the photocatalytic process. To investigate the lifetime of 40% Ag-AgBr/Al-MCM-41 catalyst, at the end of reaction, the catalyst was recovered by centrifugation, washed several times by distilled water and ethanol in the experiments. Fig. 15 revealed that the oxidative desulfurization degree of DBT decreased slightly with the recycling runs but still above 90% after recycling four times. The small amount of catalyts loss in the cyclic experiments could be the reason for the slight decrease in photocatalytic activity. However, the conversion which remained higher than 90% in all tests indicated that the Ag-AgBr/Al-MCM-41 catalyst possessed high photocatalytic stability.

In addition, XRD patterns (Fig. 16A and B) and SEM images (Fig. 16C and D) also demonstrated that there was no clear change observed in phase structure and morphology after the recycling experiments. Based on the above results, the high photocatalytic activity and stability of the Ag-AgBr/Al-MCM-41 photocatalyst could be proved.

4. Conclusions

In conclusion, various amounts of Ag-AgBr loading on Al-MCM-41 support, obtained from Vietnamese bentonite improved the surface areas of the photocatalysts by chemical deposition method using suitable amounts of CTAB. The synthesis method created a bi-functional Ag-AgBr/Al-MCM-41 with a large surface area, uniform porous structure, and an excellent photocatalytic activity for the oxidation of dibenzothiophene in model fuel samples. The optimum loading amount of Ag-AgBr on Al-MCM-41 is 40% in weight and this 40% Ag-AgBr/Al-MCM-41 material exhibits the highest photocatalytic activity, with DBT conversion of 99.22% under visible-light irradiation. Moreover, the photocatalyst maintains a high level of activity after four cycles. The synthesized nanocomposites with high photocatalytic activities could be considered as promising candidates for the effective removal of organic pollutants.

Acknowledgments

The authors acknowledge and thank the National Foundation for Sicence and Technology Development (NAFOSTED) of Vietnam (Grant No. 105.99-2015.21) for their financial support.

Appendix A. Supplementary material

Supplementary data associated with this article can be found, in the online version, at https://doi.org/10.1016/j.apt.2018.04.019.

References

[1] J. Tschirch, R. Dillert, D. Bahnemann, B. Proft, A. Biedermann, B. Goer, Photodegradation of methylene blue in water, a standard method to determine the activity of photocatalytic coatings, Res. Chem. Intermed. 34 (4) (2008) 381–392.
[2] Th. Maggos, J.G. Bartzis, M. Liakou, C. Gobin, Photocatalytic degradation of NO_x gases using TiO_2-containing paint: a real scale study, J. Hazard. Mater. 146 (3) (2007) 668–673, https://doi.org/10.1016/j.jhazmat.2007.04.079.
[3] A. Fujishima, K. Honda, Electrochemical photolysis of water at a semiconductor electrode, Nature 238 (1972) 37–38, https://doi.org/10.1038/238037a0.
[4] X. Wang, J. Chen, X. Guan, L. Gu, Enhanced efficiency and stability for visible light driven water splitting hydrogen production over $Cd_{0.5}Zn_{0.5}S$/g-C_3N_4 composite photocatalyst, Int. J. Hydrog Energy 40 (2015) 7546–7552, https://doi.org/10.1016/j.ijhydene.2014.11.055.
[5] C.-J. Chang, K.-L. Huang, J.-K. Chen, K.-W. Chu, M.-H. Hsu, Improved photocatalytic hydrogen production of ZnO/ZnS based photocatalysts by Ce doping, J. Taiwan Inst. Chem. Eng. 55 (2015) 82–89, https://doi.org/10.1016/j.jtice.2015.04.024.
[6] X. Chen, S. Shen, L. Guo, S.S. Mao, Semiconductor-based photocatalytic hydrogen generation, Chem. Rev. 110 (11) (2010) 6503–6570, https://doi.org/10.1021/cr1001645.
[7] L.G. Devi, R. Kavitha, A review on non metalnon-metal ion doped titania for the photocatalytic degradation of organic pollutants under UV/solar light: Role of photogenerated charge support dynamics in enhancing the activity, Appl. Catal. B 140–141 (2013) 559–587, https://doi.org/10.1016/j.apcatb.2013.04.035.
[8] K. Mori, P. Verma, R. Hayashi, K. Fuku, H. Yamashita, Color-controlled Ag nanoparticles and nanorods within confined mesopores: microwave-assisted rapid synthesis and application in plasmonic catalysis under visible-light irradiation, Chem.-Eur. J. 21 (2015) 11885–11893, https://doi.org/10.1002/chem.201501361.
[9] X.J. Bai, R.L. Zong, C.X. Li, D. Liu, Y.F. Liu, Y.F. Zhu, Enhancement of visible photocatalytic activity via Ag@C_3N_4 core–shell plasmonic composite, Appl. Catal. B-Environ. 147 (2014) 82–91, https://doi.org/10.1016/j.apcatb.2013.08.007.
[10] Z. Bian, T. Tachikawa, P. Zhang, M. Fujitsuka, T. Majima, Au/TiO_2 Superstructure based plasmonic photocatalysts exhibiting efficient charge separation and unprecedented activity, J. Am. Chem. Soc. 136 (2014) 458–465, https://doi.org/10.1021/ja410994f.
[11] P. Wang, B. Huang, X. Zhang, X. Qin, H. Jin, Y. Dai, Z. Wang, J. Wei, J. Zhan, S. Wang, J. Wang, M.H. Whangbo, Highly efficient visible-light plasmonic photocatalyst Ag@AgBr, Chem.-Eur. J. 15 (2009) 1821–1824, https://doi.org/10.1002/chem.200802327.
[12] J. Jiang, H. Li, L. Zhang, New insight into daylight photocatalysis of AgBr@Ag: synergistic effect between semiconductor photocatalysis and plasmonic photocatalysis, Chem.-Eur. J. 18 (2012) 6360–6369, https://doi.org/10.1002/chem.201102606.
[13] X. Xiao, L. Ge, C. Han, Y. Li, Z. Zhao, Y. Xin, S. Fang, L. Wu, P. Qiu, A facile way to synthesize Ag@AgBr cubic cages with efficient visible-light-induced photocatalytic activity, Appl. Catal. B-Environ. 163 (2015) 564–572, https://doi.org/10.1016/j.apcatb.2014.08.037.
[14] P. Wang, B. Huang, X. Qin, X. Zhang, Y. Dai, J. Wei, M.H. Whangbo, Ag@AgCl: A highly efficient and stable photocatalyst active under visible light, Angew. Chem. Int. Ed. 47 (2008) 7931–7933, https://doi.org/10.1002/anie.200802483.
[15] Z. Zheng, C. Chen, A. Bo, F.S. Zavahir, E.R. Waclawik, J. Zhao, D. Yang, H. Zhu, Visible-light-induced selective photocatalytic oxidation of benzylamine into imine over supported Ag/AgI photocatalysts, Chem. Cat. Chem 6 (2014) 1210–1214, https://doi.org/10.1002/cctc.201301030.
[16] Y. Zhao, L. Kuai, B. Geng, Low-cost and highly efficient composite visible light-driven Ag–AgBr/γ-Al_2O_3 plasmonic photocatalyst for degrading organic pollutants, Catal. Sci. Technol. 2 (2012) 1269–1274, https://doi.org/10.1039/C2CY20074K.
[17] R.K. Roy, S. Bandyopadhyaya, A.K. Pal, Surface plasmon resonance in nanocrystalline silver in a ZnO matrix, Eur. Phys. J. B 39 (2004) 491–498, https://doi.org/10.1140/epjb/e2004-00222-x.
[18] D.S. Wang, Y.D. Duan, Q.Z. Luo, X.Y. Li, J. An, L.L. Bao, L. Shi, Novel preparation method for a new visible light photocatalyst: mesoporous TiO_2 supported Ag/

AgBr, J. Mater. Chem. 22 (2012) 4847–4854, https://doi.org/10.1039/C2JM14628B.
[19] J.G. McEvoy, Z.S. Zhang, Synthesis and characterization of Ag/AgBr–activated carbon composites for visible light induced photocatalytic detoxification and disinfection, J. Photo. Chem. Photobiol. A-Chem. 321 (2016) 161–170, https://doi.org/10.1016/j.jphotochem.2016.02.004.
[20] Y. Xu, H. Xu, J. Yan, H. Li, L. Huang, Q. Zhang, C. Huang, H. Wan, A novel visible light response plasmonic photocatalyst CNT/Ag/AgBr and its photocatalytic properties, PCCP 15 (2013) 5821–5830, https://doi.org/10.1039/c3cp44104k.
[21] M. Zhu, P. Chen, M. Liu, Ag/AgBr/graphene oxide nanocomposite synthesized via oil/water and water/oil microemulsions: a comparison of sunlight energized plasmonic photocatalytic activity, Langmuir 28 (2012) 3385–3390, https://doi.org/10.1021/la204452p.
[22] C. Hu, Y.Q. Lan, J.H. Qu, X.X. Hu, A.M. Wang, Ag/AgBr/TiO_2 visible light photocatalyst for destruction of azo dyes and bacteria, J. Phys. Chem. B 110 (2006) 4066–4072, https://doi.org/10.1021/jp0564400.
[23] H. Liang, C. Li, J. Bai, J. Wang, A. Shan, L. Guo, D. Yu, Fabrication of visible-light-responsed calcium metasilicate-supported Ag–AgX/TiO2 (X = Cl, Br, I) composites and their photocatalytic properties, Adv. Powder Technol. 26 (2015) pp. 1005–1012. 10.1016/j.apt.2015.04.006.
[24] Y. Bi, J. Ye, In – situ oxidation synthesis of Ag/AgCl core–shell nanowires and their photocatalytic properties, Chem. Commun. 43 (2009) 6551–6553, https://doi.org/10.1039/B913725D.
[25] W.S. Choi, G.Y. Byun, T.S. Bae, H. Lee, Evolution of AgX nanowires into Ag derivative nano/microtubes for highly efficient visible-light photocatalysts, ACS Appl. Mater. Interfaces 5 (2013) 11225–11233, https://doi.org/10.1021/am4034735.
[26] Y. Tang, Z. Dong, Z. Chen, Z. Jiang, G. Xing, A.K.P. Li, Y. Zhang, T.C. Sum, S. Li, X. Chen, Efficient Ag@AgCl cubic cage photocatalysts profit from ultrafast plasmon-induced electron transfer processes, Adv. Funct. Mater. 23 (2013) 2932–2940, https://doi.org/10.1002/adfm.201203379.
[27] Y. Liu, J. Goebl, Y. Yin, Templated synthesis of nanostructured materials, Chem. Soc. Rev. 42 (2013) 2610–2653, https://doi.org/10.1039/C2CS35369E.
[28] S. Lou, X. Jia, Y. Wang, S. Zhou, Template-assisted in-situ synthesis of porous AgBr/Ag composite microspheres as highly efficient visible-light photocatalyst, Appl. Catal. B Environ. 176–177 (2015) 586–593, https://doi.org/10.1016/j.apcatb.2015.04.027.
[29] N.K. Nga, P.T.T. Hong, T.D. Lam, T.Q. Huy, A facile synthesis of nanostructured magnesium oxide particles for enhanced adsorption performance in reactive blue 19 removal, J. Colloid Interface Sci. 398 (2013) pp. 210–216. 10.1016/j.jcis.2013.02.018.
[30] H. Yang, Y. Deng, C. Du, S. Jin, Novel synthesis of ordered mesoporous materials Al-MCM-41 from bentonite, Appl. Clay Sci. 47 (2010) 351–355, https://doi.org/10.1016/j.clay.2009.11.050.
[31] T. Ali-dahmane, M. Adjdir, R. Hamacha, F. Villieras, A. Bengueddach, P.G. Weidler, The synthesis of MCM-41 nanomaterial from Algerian Bentonite: The effect of the mineral phase contents of clay on the structure properties of MCM-41, C. R. Chimie 17 (2014) pp. 1–6. 10.1016/j.crci.2012.12.017.
[32] J. Robertson, T.J. Bandosz, Photooxidation of dibenzothiophene on TiO_2/hectorite thin films layered catalyst, J. Colloid Interface Sci. 299 (1) (2006) 125–135, https://doi.org/10.1016/j.jcis.2006.02.011.
[33] H. Misran, R. Singh, S. Begum, M.A. Yarmo, Processing of mesoporous silica materials (MCM-41) from coal fly ash, J. Mater. Process. Tech. 186 (2007) 8–13, https://doi.org/10.1016/j.jmatprotec.2006.10.032.
[34] B. Marler, U. Oberhagemaan, S. Vortmaan, H. Gies, Influence of the sorbate type on the XRD peak intensities of loaded MCM-41, Micropor. Mater. 6 (1996) 375–383, https://doi.org/10.1016/0927-6513(96)00016-8.
[35] C.-M. Yang, P.-H. Liu, Y.-F. Ho, C.-Y. Chiu, K.-J. Chao, Highly dispersed metal nanoparticles in functionalized SBA-15, Chem. Mater. 15 (2003) 275–280, https://doi.org/10.1021/cm020822q.
[36] P. Shah, A.V. Ramaswamy, K. Lazar, Veda Ramaswamy, Direct hydrothermal synthesis of mesoporous Sn-SBA-15 materials under weak acidic conditions, Micropor. Mesopor. Mater. 100 (2007) 210–226, https://doi.org/10.1016/j.micromeso.2006.10.042.
[37] P.R. Selvakannan, K. Mantri, J. Tardio, S.K. Bhargava, High surface area Au–SBA-15 and Au–MCM-41 materials synthesis: Tryptophan amino acid mediated confinement of gold nanostructures within the mesoporous silica pore walls, J. Colloid Interface Sci. 394 (2013) 475–484, https://doi.org/10.1016/j.jcis.2012.12.008.
[38] M.N. Timofeeva, S.H. Jhung, Y.K.H. Wang, D.K. Kim, V.N. Panchenko, M.S. Melgunov, Yu.A. Chesalov, J.S. Chang, Ce-silica mesoporous SBA-15- type materials for oxidative catalysis: Synthesis, characterization, and catalytic application, Appl. Catal. A Gen. 317 (2007) 1–10, https://doi.org/10.1016/j.apcata.2006.07.014.
[39] L. Kuai, B. Geng, X. Chen, Y. Zhao, Y. Luo, Facile subsequently light-induced route to highly efficient and stable sunlight-driven Ag-AgBr plasmonic photocatalyst, Langmuir 26 (2010) 18723–18727, https://doi.org/10.1021/la104022g.
[40] A. Esmaeili, M.H. Entezari, Sonosynthesis of an Ag/AgBr/Graphene-oxide nanocomposite as a solar photocatalyst for efficient degradation of methyl orange, J. Colloid Interface Sci. 466 (2016) 227–237, https://doi.org/10.1016/j.jcis.2015.12.034.
[41] C.H. An, J.Z. Wang, W. Jiang, M.Y. Zhang, X.J. Ming, S.T. Wang, Q.H. Zhang, Strongly visible-light responsive plasmonic shaped AgX: Ag (X = Cl, Br) nanoparticles for reduction of CO_2 to methanol, Nanoscale 4 (2012) 5646–5650, https://doi.org/10.1039/c2nr31213a.
[42] X. Wang, Y. Tang, Z. Chen, T.-T. Lim, Highly stable heterostructured Ag-AgBr/TiO_2 composite: A bifunctional visible-light active photocatalyst for destruction of ibuprofen and bacteria, J. Mater. Chem. 22 (2012) 23149–23158, https://doi.org/10.1039/c2jm35503e.
[43] X. Liu, D. Zhang, B. Guo, Y. Qu, G. Tian, H. Yue, S. Feng, Recyclable and visible light sensitive Ag–AgBr/TiO_2: Surface adsorption and photodegradation of MO, Appl. Surf. Sci. 353 (2015) 913–923, https://doi.org/10.1016/j.apsusc.2015.06.206.
[44] P. Trongkaew, T. Utistham, P. Reubroycharoen, N. Hinchiranan, Photocatalytic desulfurization of waste tire pyrolysis oil, Energies 4 (2011) 1880–1896, https://doi.org/10.3390/en4111880.
[45] T. Hirai, K. Ogawa, I. Komasawa, Desulfurization process for dibenzothiophenes from light oil by photochemical reaction and liquid–liquid extraction, Ind. Eng. Chem. Res. 35 (1996) 586–589, https://doi.org/10.1021/ie9503407.
[46] D. Zhao, J. Zhang, J. Wang, W. Liang, H. Li, Photocatalytic oxidation desulfurization of diesel oil using Ti-containing zeolite, Petrol. Sci. Technol. 27 (2009) 1–11, https://doi.org/10.1080/10916460802108314.
[47] Y. Yang, G. Zhang, Preparation and photocatalytic properties of visible light driven Ag-AgBr/attapulgite nanocomposite, Appl. Clay Sci. 67–68 (2012) 11–17. http://doi:10.1016/j.clay.2012.06.013.